NASA/CR—2003-212388

Nonlinear Aeroacoustics Computations by the Space-Time CE/SE Method

Ching Y. Loh
Taitech, Inc., Beaver Creek, Ohio

June 2003

The NASA STI Program Office . . . in Profile

Since its founding, NASA has been dedicated to the advancement of aeronautics and space science. The NASA Scientific and Technical Information (STI) Program Office plays a key part in helping NASA maintain this important role.

The NASA STI Program Office is operated by Langley Research Center, the Lead Center for NASA's scientific and technical information. The NASA STI Program Office provides access to the NASA STI Database, the largest collection of aeronautical and space science STI in the world. The Program Office is also NASA's institutional mechanism for disseminating the results of its research and development activities. These results are published by NASA in the NASA STI Report Series, which includes the following report types:

- TECHNICAL PUBLICATION. Reports of completed research or a major significant phase of research that present the results of NASA programs and include extensive data or theoretical analysis. Includes compilations of significant scientific and technical data and information deemed to be of continuing reference value. NASA's counterpart of peer-reviewed formal professional papers but has less stringent limitations on manuscript length and extent of graphic presentations.

- TECHNICAL MEMORANDUM. Scientific and technical findings that are preliminary or of specialized interest, e.g., quick release reports, working papers, and bibliographies that contain minimal annotation. Does not contain extensive analysis.

- CONTRACTOR REPORT. Scientific and technical findings by NASA-sponsored contractors and grantees.

- CONFERENCE PUBLICATION. Collected papers from scientific and technical conferences, symposia, seminars, or other meetings sponsored or cosponsored by NASA.

- SPECIAL PUBLICATION. Scientific, technical, or historical information from NASA programs, projects, and missions, often concerned with subjects having substantial public interest.

- TECHNICAL TRANSLATION. English-language translations of foreign scientific and technical material pertinent to NASA's mission.

Specialized services that complement the STI Program Office's diverse offerings include creating custom thesauri, building customized databases, organizing and publishing research results . . . even providing videos.

For more information about the NASA STI Program Office, see the following:

- Access the NASA STI Program Home Page at ***http://www.sti.nasa.gov***

- E-mail your question via the Internet to help@sti.nasa.gov

- Fax your question to the NASA Access Help Desk at 301–621–0134

- Telephone the NASA Access Help Desk at 301–621–0390

- Write to:
  NASA Access Help Desk
  NASA Center for AeroSpace Information
  7121 Standard Drive
  Hanover, MD 21076

NASA/CR—2003-212388

Nonlinear Aeroacoustics Computations by the Space-Time CE/SE Method

Ching Y. Loh
Taitech, Inc., Beaver Creek, Ohio

Prepared for the
Regional Research Conference: Mathematical Methods in Nonlinear Wave Propagation
cosponsored by the National Science Foundation and the Conference Board
of the Mathematical Sciences
Greensboro, North Carolina, May 15–19, 2002

Prepared under Contract NAS3–03072

National Aeronautics and
Space Administration

Glenn Research Center

June 2003

This report contains preliminary findings, subject to revision as analysis proceeds.

The Propulsion and Power Program at
NASA Glenn Research Center sponsored this work.

Available from

NASA Center for Aerospace Information
7121 Standard Drive
Hanover, MD 21076

National Technical Information Service
5285 Port Royal Road
Springfield, VA 22100

Available electronically at http://gltrs.grc.nasa.gov

Nonlinear Aeroacoustics Computations by the Space-Time CE/SE Method

Ching Y. Loh
Taitech, Inc.
Beaver Creek, Ohio 45430

1. Introduction

The Space-Time Conservation Element and Solution Element Method, or CE/SE Method for short [1-3], is a recently developed numerical method for conservation laws. Despite its second order accuracy in space and time, it possesses low dispersion errors and low dissipation. The method is robust enough to cover a wide range of compressible flows: from weak linear acoustic waves to strong discontinuous waves (shocks). An outstanding feature of the CE/SE scheme is its truly multi-dimensional, simple but effective non-reflecting boundary condition (NRBC), which is particularly valuable for CAA (computational aeroacoustics).

In nature, the method may be categorized as a finite volume method, where the conservation element (CE) is equivalent to a finite control volume (or cell) and the solution element (SE) can be understood as the cell interface. However, due to its careful treatment of the surface fluxes and geometry, it is different from the existing schemes.

Currently, the CE/SE scheme has been developed to a matured stage that a 3-D unstructured CE/SE Navier-Stokes solver is already available. However, in the present review paper, as a general introduction to the CE/SE method, only the 2-D unstructured Euler CE/SE solver is chosen and sketched in §2. Then applications of the 2-D and 3-D CE/SE schemes to linear, and in particular, nonlinear aeroacoustics are depicted in § 3, § 4, and § 5 to demonstrate its robustness and capability.

2. The 2-D CE/SE Euler Scheme

In this Section, only a brief sketch of the CE/SE scheme for the 2-D Euler equations for gas dynamics is given. Detailed description of the method may be found in the original papers [1- 3].

2.1. Conservation Form of the 2-D Unsteady Euler Equations. Consider a dimensionless conservation form of the unsteady 2-D Euler equations of a perfect gas. Let ρ, u, v, p, and γ be the density, streamwise and transverse velocity components, static pressure, and constant specific heat ratio, respectively. The 2-D

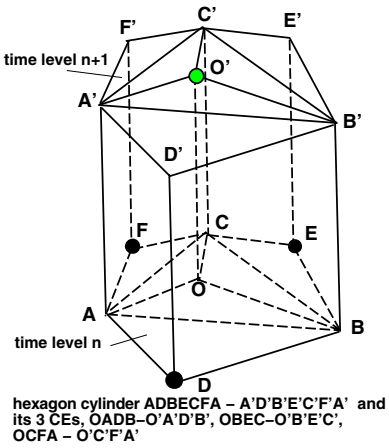

FIGURE 1. CE/SE unstructured grid in space-time E_3 space.

Euler equations then can be written in the following vector form:

$$\mathbf{U_t} + \mathbf{F_x} + \mathbf{G_y} = \mathbf{0}, \tag{1}$$

where x, y, and t are the streamwise and transversal coordinates and time, respectively. The conservative flow variable vector $\mathbf{U}$ and the flux vectors in the streamwise and radial directions, $\mathbf{F}$ and $\mathbf{G}$, are given by:

$$\mathbf{U} = \begin{pmatrix} U_1 \\ U_2 \\ U_3 \\ U_4 \end{pmatrix}, \quad \mathbf{F} = \begin{pmatrix} F_1 \\ F_2 \\ F_3 \\ F_4 \end{pmatrix}, \quad \mathbf{G} = \begin{pmatrix} G_1 \\ G_2 \\ G_3 \\ G_4 \end{pmatrix},$$

with the conservative flow variables

$$U_1 = \rho, \quad U_2 = \rho u, \quad U_3 = \rho v, \quad U_4 = p/(\gamma - 1) + \rho(u^2 + v^2)/2.$$

where the fluxes are:

$$F_1 = U_2, \quad F_2 = (\gamma - 1)U_4 + \left[(3 - \gamma)U_2^2 - (\gamma - 1)U_3^2\right]/2U_1,$$
$$F_3 = U_2U_3/U_1, \quad F_4 = \gamma U_2U_4/U_1 - (\gamma - 1)U_2\left[U_2^2 + U_3^2\right]/2U_1^2,$$
$$G_1 = U_3, \quad G_2 = U_2U_3/U_1, \quad G_3 = (\gamma - 1)U_4 + \left[(3 - \gamma)U_3^2 - (\gamma - 1)U_2^2\right]/2U_1,$$
$$G_4 = \gamma U_3U_4/U_1 - (\gamma - 1)U_3\left[U_2^2 + U_3^2\right]/2U_1^2.$$

By considering (x, y, t) as coordinates of a three-dimensional Euclidean space, E_3, and using Gauss' divergence theorem, it follows that Eq. (1) is equivalent to the following integral conservation law:

$$\oint_{S(V)} \mathbf{H_m} \cdot \mathrm{d}\mathbf{S} = \mathbf{0}, \qquad \mathbf{m} = \mathbf{1}, \mathbf{2}, \mathbf{3}, \mathbf{4}, \tag{2}$$

where $S(V)$ denotes the surface around a volume V in E_3 and $\mathbf{H_m} = (\mathbf{F_m}, \mathbf{G_m}, \mathbf{U_m})$.

In general, the CE/SE method systematically the *integral* equations (2) and naturally captures shocks and other discontinuities in the flow. Both conservative variables $\mathbf{U}$ and their spatial derivatives $\mathbf{U}_x$, $\mathbf{U}_y$ are computed simultaneously as unknowns.

2.2. Unstructured Grid for CE/SE. The CE/SE scheme is constructed to take advantage of an unstructured triangular grid. The unstructured geometry used with the CE/SE scheme is illustrated in Fig. 1. Here, ΔABC is a typical triangle cell and D, E, F are the triangle centers of the neighboring cells. The flow variables $\mathbf{U}$, $\mathbf{U}_x$, and $\mathbf{U}_y$ at the previous time step are stored at the triangle cell centers. Three quadrilateral cylinders (conservation elements) are formed by the edges that connect the vertices and the center of the triangle and its three neighbors. In the space-time E_3 space, Eq. (2) is applied to the hexagon cylinder $ADBECF - A'D'B'E'C'F'$ of volume V that consists of these 3 quadrilateral cylinder CEs (Fig 1).

In the CE/SE scheme, the above flux conservation relation, Eq. (2), in space-time is the *only* mechanism that transfers information between node points. A conservation element CE (here, quadrilateral cylinders) is the finite volume to which Eq. (2) is applied. Discontinuities are allowed to occur in a conservation element. A solution element SE associated with a grid node (*e.g.*, D, E, or F in Fig. 1) is here a set of interface planes in E_3 that passes through this node (*e.g.* $DAA'D'$, $DBB'D'$, $EBB'E'$, $ECC'E'$, etc.). Each surface $S(CE)$ is made up of segments belonging to *two* neighboring CE's. Within a given solution element $SE(j,n)$, where j, n are the node index and time step, respectively, the flow variables are not only considered continuous but are also approximated by the linear Taylor series expansions. The surface flux can thus be calculated accurately and easily by first evaluating the flux vectors at the geometrical center of the surface through the above Taylor series expansions.

At time level n, the solution variables $\mathbf{U}$, $\mathbf{U_x}$, and $\mathbf{U_y}$ are given at the three nodes D, E, F in Fig. 1 and $\mathbf{U}$, $\mathbf{U_x}$ and $\mathbf{U_y}$ at O' at the new time level $n+1$ are to be evaluated. In principle, each of the 3 CEs provides 4 scalar equations when Eq. (2) is applied to the element. Hence, the 12 scalar equations needed for the 12 scalar unknowns at O' are available. All the unknowns are computed based on these relations. No extrapolations (interpolations) across a stencil of cells are needed.

2.3. Non-Reflecting Boundary Conditions (NRBCs) for CE/SE. In the CE/SE scheme, NRBCs are constructed so as to allow fluxes remain continuous across the boundary surfaces. For example, at the downstream boundary, where there are substantial gradients in y direction, the NRBC requires that

$$(\mathbf{U}_x)_j^n = 0,\ \mathbf{U}_j^n = \mathbf{U}_{j'}^{n-1/2}\ (\mathbf{U}_y)_j^n = (\mathbf{U}_y)_{j'}^{n-1/2},$$

where j' is the index of an interior node closest to the boundary ghost node j and $\mathbf{U}_j^n$ and $(\mathbf{U}_y)_j^n$ are now defined by simple extrapolation from the interior. This NRBC is valid for either supersonic or subsonic flows.

In the following sections, the 2-D and 3-D CE/SE Euler (Navier-Stokes) schemes are tested to demonstrate its capability and robustness for aeroacoustics computations. Several selected problems in linear and nonlinear aeroacoustics computations are presented. The numerical results, which cover a wide spectrum of waves, from linear and nonlinear acoustic waves to discontinuous waves (shocks), are then compared to available exact solutions or experimental findings.

3. 2-D Linear Aeroacoustics Test Problems

Three typical linear aeroacoustics examples are considered in this section. More details can be found in [5, 6].

3.1. Acoustic Pulse, Entropy Wave, and Vorticity Wave Propagation. This problem [5] is one of the benchmark problems of the first CAA Workshop (Category 3, Problem 1) [4]. The computational domain in the x-y plane is a square with $-100 \leq x \leq 100$, and $-100 \leq y \leq 100$. A uniform 201×201 grid is used with $\Delta x = \Delta y = 1$. Initially, a Gaussian acoustic pulse is located at the center of the domain (0,0) and a weaker entropy/vorticity disturbance is located off center (67,0), with a mean flow of Mach number $M = 0.5$ in the x direction. The corresponding non-dimensional pressure, density, and streamwise and transverse velocity components are given by

$$p = \frac{1}{\gamma} + \delta \mathrm{e}^{-\alpha_1(x^2+y^2)}, \quad \rho = 1 + \delta[\mathrm{e}^{-\alpha_1(x^2+y^2)} + 0.1\delta \mathrm{e}^{-\alpha_2[(x-67)^2+y^2]}],$$

$$u = M + 0.04\delta y \mathrm{e}^{-\alpha_2[(x-67)^2+y^2]}, \quad v = -0.04\delta(x-67)\mathrm{e}^{-\alpha_2[(x-67)^2+y^2]},$$

where $\alpha_1 = \ln 2/9$, $\alpha_2 = \ln 2/25$, and δ is an amplitude factor. By choosing a small $\delta = 0.001$, the Euler equations are practically linearized. During the computation, the NRBC of Type-I described above is enforced at all boundaries. Fig. 2 illustrates the density contours at different time steps. It also shows that the simple NRBC is effective. Comparison of perturbed density distributions along the centerline $y = 0$ with the exact solutions at $t = 60$ and $t = 100$ are demonstrated in Plots (a) and (b) respectively. The numerical results agree well with the theoretical ones, with no visible dispersion error.

3.2. Linear Instability of a Free Shear Layer and Vortex Roll-Up. In the 2nd example [5], the inviscid linear and nonlinear instability properties of a free shear layer is studied. The numerical results are compared with linear results obtained by the normal mode approach.

The background mean flow consists of a fast (supersonic) stream on the top half domain and a slow (subsonic) stream at the bottom half, with the two parallel streams connected by a shear layer of hyperbolic tangent shape. The nondimensional flow states are given as:

$$U_1 = 1, V_1 = 0, \quad p_1 = 1/3.15, \quad \rho_1 = 1,$$

$$U_2 = .7391304,\ V_2 = 0,\ p_2 = 1/3.15,\ \rho_2 = 0.5405405.$$

The computational domain spans between $0 \leq x \leq 300$ and $-10 \leq y \leq 10$, with a uniform structured grid of 601×101 (1201×201 for fine grid), with time step size $\Delta t = 0.15$. The computation is carried out until $t = 390$ when the spatial instability is fully developed. A small harmonic perturbation (amplitude $\delta = 0.001$) at the most unstable frequency $f = 0.062$ is enforced at the inlet boundary. Fig. 3 shows the power spectrum P_n of the computed u' (perturbation of u) in natural log scale at the streamwise stations $x = 50$, 100, 150, and 250, which correspond to about 3.5, 7 wavelengths and so on. At $x = 50$, there is a clearly discernible peak centered at about the forcing frequency $f = 0.062$. At about $x = 100$, second and third harmonics start to emerge. Further downstream, more harmonics appear and eventually the fundamental saturates. The streamwise evolution of the disturbance amplitude along the horizontal centerline $y = 0$ is illustrated in

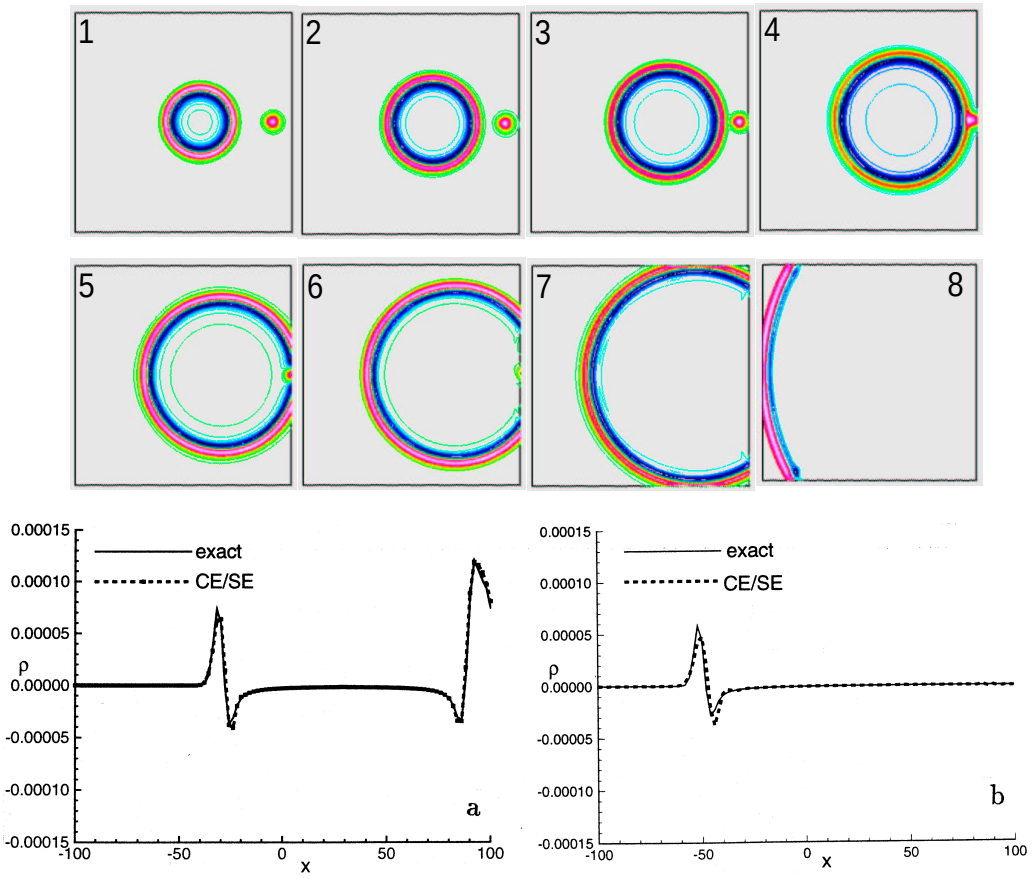

FIGURE 2. Propagation of an acoustic pulse with a vorticity/entropy disturbance, and comparison to exact solution.

Fig 4. Numerical results for both the coarse and fine grids are presented and compared to the theoretical linear growth. It is seen that for $0 \leq x \leq 100$ (about 7 wavelengths) the coarse-grid and fine-grid computations yield good agreement both between themselves and with the linear result. Further downstream, nonlinear effects become important, the growth rate is reduced from the linear value, and ultimately the fundamental saturates. Both numerical results agree reasonably well with each other also in this nonlinear region. Fig. 5 shows the streamwise evolution of the disturbance phase. The numerical results for both the coarse and finer grids are compared to the corresponding result from linear theory. The agreement is surprisingly good until well into the nonlinear region. Fig. 6 compares the normalized $|u'|$ profile across the shear layer flow with the eigenfunction from linear stability theory at the streamwise station $x = 100$, which is located towards the end of the linear growth region. The agreement is excellent. The phase variation across the shear layer of the disturbance at the same station is depicted in Fig. 7.

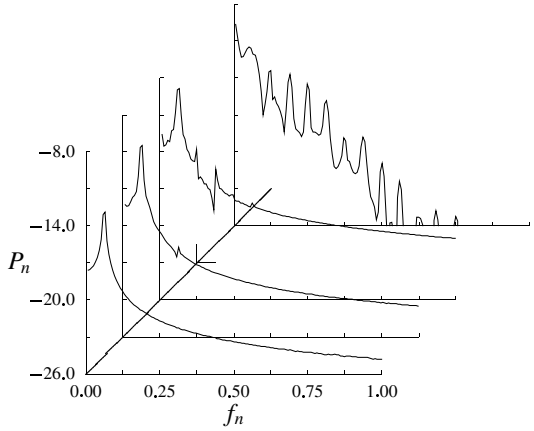

FIGURE 3. Power spectra at x = 050, 100, 150, and 250 with forcing at the most unstable frequency according to linear theory; (coarse grid)

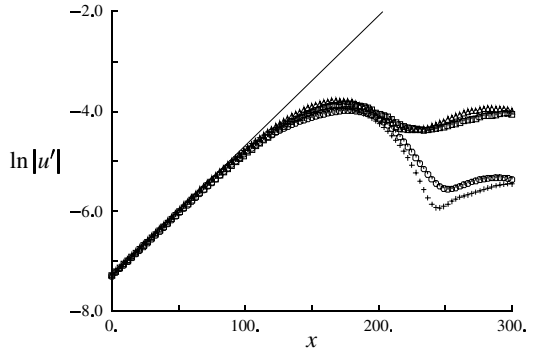

FIGURE 4. Streamwise evolution of disturbance amplitude with forcing at the most unstable frequency according to linear theory (f = .062). Squares: total u_{rms}, coarse grid; triangles: total u_{rms}, finer grid; circles: u_{rms} at forcing frequency, coarse grid; crosses: u_{rms} at forcing frequency, finer grid; solid line: linear growth.

Fig. 8 shows the contours of the flow variables for the finer-grid computation. This figure clearly demonstrates the effectiveness of the NRBC's at the top, bottom and outlet. It should be emphasized that the domain shown in the figures is exactly the computational domain, no buffer zones, cut-offs or other numerical fixes are applied.

3.3. Mach radiation from a supersonic axisymmetric jet. Another interesting linear or quasi-linear wave phenomenon is the Mach radiation from a fully expanded supersonic jet. In the following examples, a perturbation (or forcing) is

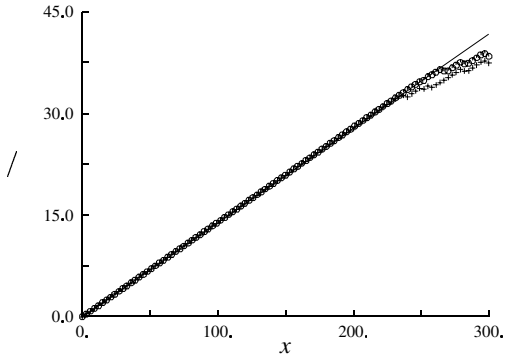

FIGURE 5. Streamwise evolution of disturbance phase with forcing at the most unstable frequency according to linear theory (f=.062). Circles: coarse grid; crosses: finer grid; solid line: linear result.

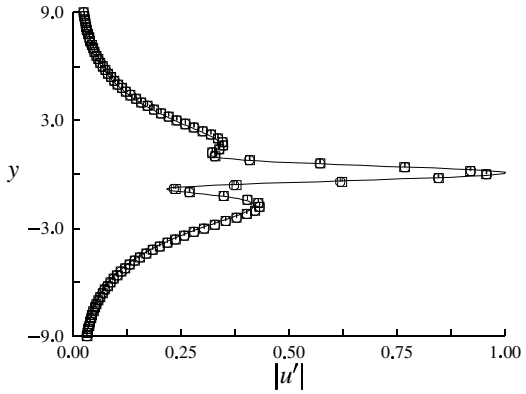

FIGURE 6. Transverse mode shape at $x = 100$ with forcing at most unstable frequency according to linear theory, finer grid. Squares: total u_{rms}; circles: u_{rms} at forcing frequency; solid line: linear eigenfunction (modulus).

provided by a right-hand-side source term in the energy equation, the 4th component of Eq. (1), located at the origin $(0, 0)$ inside the jet core:

$$\frac{\delta}{\gamma - 1} \exp[-B(x^2 + y^2)] \cos(\omega t),$$

where $\delta = 0.001$ is a small number, $\omega = 2\pi St$ (St being the Strouhal number), and the constant $B = 8$. In this test example [6], a fully expanded supersonic jet with Mach number $M_j = 2.0$ is considered. The computational domain spans between $0 \leq x \leq 33D$ and $0 \leq y \leq 19D$, with a non-uniform structured grid of 350×281 nodes, where D is the diameter of the jet at the nozzle exit. More grid points are packed around the shear layer. The computation of the unsteady jet flow is carried out to $t = 100$ when the spatial instability is fully developed. Fig. 9 illustrates the isobars and v-velocity contours in the near and intermediate

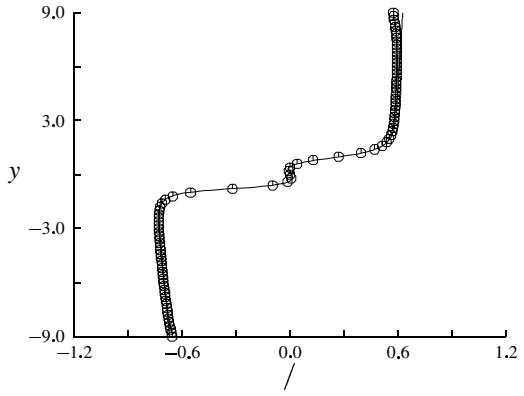

FIGURE 7. Transverse phase variation at $x = 100$ with forcing at most unstable frequency $f = .062$ according to linear theory, (fine grid). Circles: u_{rms} at forcing frequency; solid line: linear eigenfunction (phase).

field. The Mach radiation flow pattern agrees qualitatively with experimental [7] and other computational [8] results.

4. 2-D Nonlinear aeroacoustics Test problems

In this section, several examples of non-linear aeroacoustics involving shocks are demonstrated to show the capability of the CE/SE scheme.

4.1. Multiple Interaction of a Strong Vortex and Shocks. Vortex-shock interaction has been considered a 'difficult' problem for CAA , since most of the CAA schemes handle weak acoustic waves and srong socks simultaneously. However, the CE/SE Euler scheme can solve the problem in an effortless way, without any numerical trick or fix [5]. As seen in Fig 10, a uniform structured grid of 401×101 nodes is employed in the rectangular domain with $\Delta x = \Delta y = 1$. The inflow boundary condition is given as a supersonic flow with a Mach number of 2.9:

$$u_0 = 2.9, \quad v_0 = 0, \quad p_0 = 1/1.4, \quad \rho_0 = 1.$$

The boundary condition at the top is an inclined flow:

$$u_t = 2.6193, \; v_t = -0.50632, p_t = 1.5282, \; \rho_t = 1.7000.$$

The outflow boundary condition is the type-II NRBC and the bottom is a solid reflecting wall. Then, a steady oblique shock is formed with 29^o inclination and reflected at the bottom wall. The flow with shocks is pre-calculated until a steady state is reached. It is then used as the background mean flow for further computation.

At $t = 0$, a strong Lamb's vortex is placed at (22,60) (Fig. 10). With $\Delta t = 0.2$, 900 time steps were run. Fig. 10 demonstrates the shock-vortex interaction at the different times $t = 2$, 20, 38, 56, 74, 92, 110, 128, 146, and 180, and shows how the nonlinear acoustic waves are generated, and how they pass through the shocks and convect downstream.

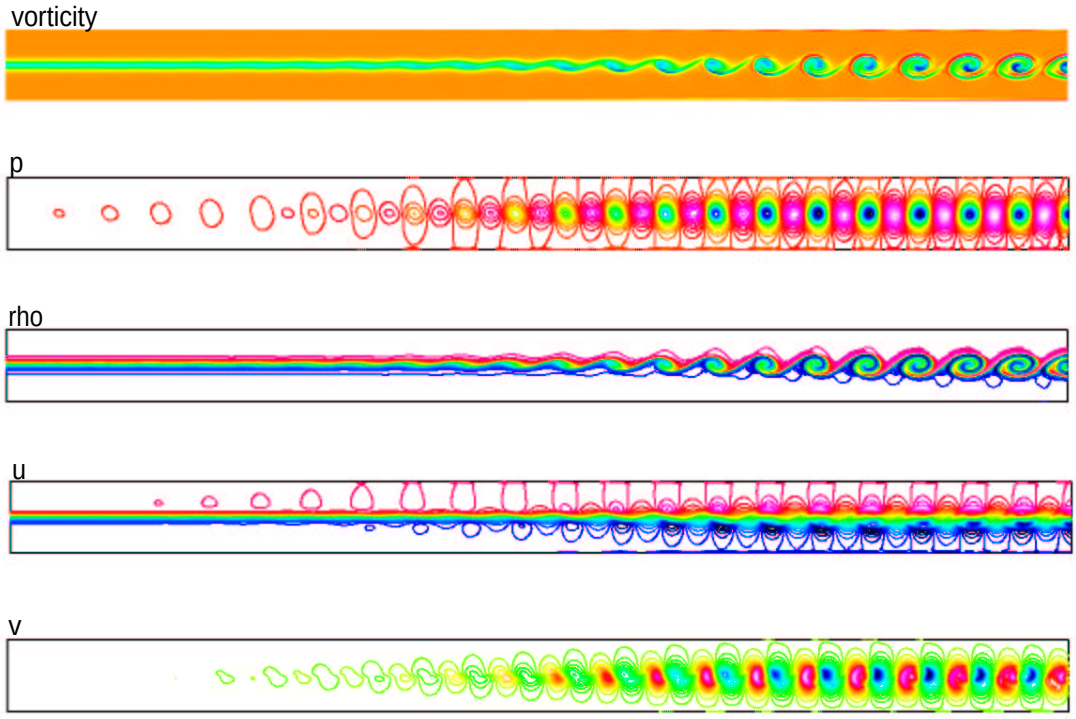

FIGURE 8. Flow variable contours at $t = 390$, fine grid

4.2. Screech tone noise of an axisymmetric underexpanded jet. Screech tone noise is a typical nonlinear aeroacoustic phenomenon. In nature, the screech noise is caused by an acoustic feedback loop between the jet nozzle exit lip (or nearby solid surfaces) and the shock cell structure. At the low supersonic jet Mach number $M_j = 1.19$, the overall motion in the experiment [8] is in an axisymmetric mode, and the use of an axisymmetric 2-D scheme is appropriate.

The Navier-Stokes CE/SE solver with LES (large eddy simulation) is applied to a triangulated grid of 88300 cells [10]. The geometry of the computational domain is shown in Fig 11. Both Type I and II NRBC's are applied appropriately to all boundaries except at the nozzle solid walls where no-slip solid wall boundary condition is employed, and at the nozzle exit where the following inflow condition is applied:

$$p_e = p_0 \left[\frac{1 + \frac{1}{2}(\gamma - 1)M_j^2}{1 + \frac{1}{2}(\gamma - 1)} \right]^{\frac{\gamma}{\gamma - 1}}, \quad \rho_e = 0.5(\gamma + 1)\rho_0 \left[\frac{1 + \frac{1}{2}(\gamma - 1)M_j^2}{1 + \frac{1}{2}(\gamma - 1)} \right]^{\frac{\gamma}{\gamma - 1}},$$

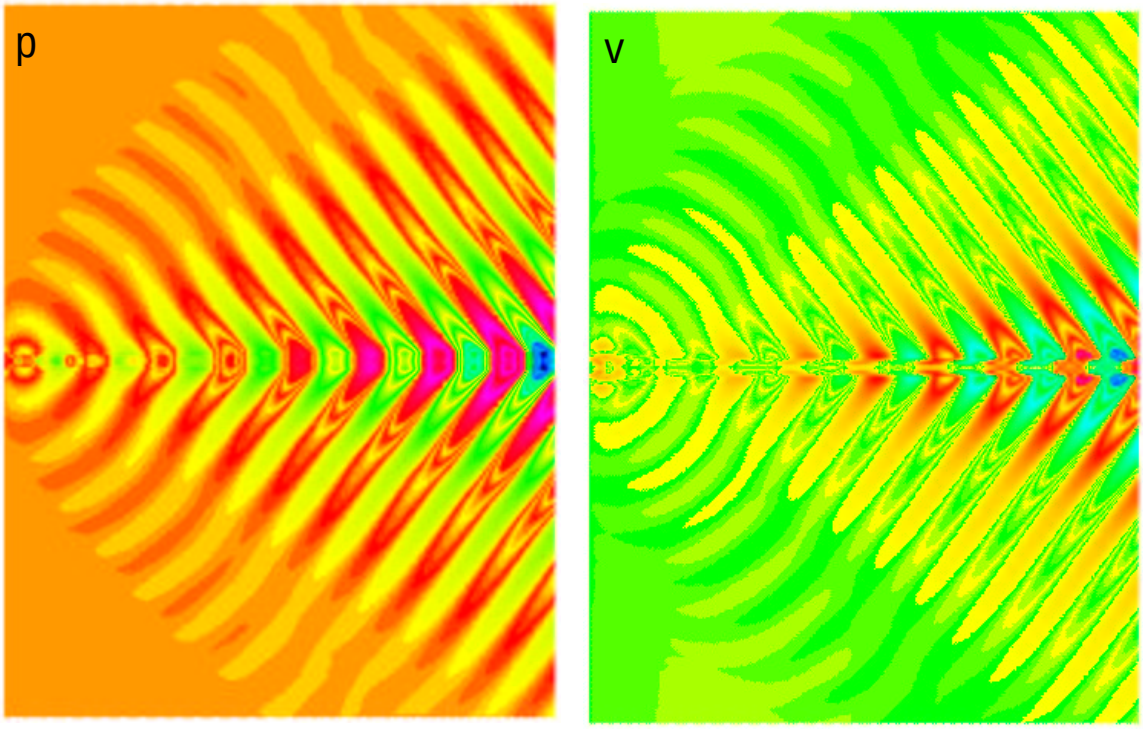

FIGURE 9. Mach radiation of a supersonic jet at $M_j = 2.0$ and Strouhal number $St = 0.2$, domain size 33Dx19D, non-uniform grid.

$$u_e = (\frac{2}{(\gamma+1)})^{1/2}, v_e = 0.$$

Initially the entire field is set to the quiescent ambient flow:

$$\rho_0 = 1, \quad u_0 = 0, \quad v_0 = 0, \quad p_0 = \frac{1}{\gamma}.$$

In the numerical simulation, the initial impact of the boundary condition at the nozzle exit will stimulate the jet shear layer and trigger the feedback loop to form the self-sustaining oscillation that generates screech waves. Fig. 13 illustrates the radiating screech waves at the time level of 410,000 steps. Since there is no forcing at all, these waves are a sure sign of the presence of a sustainable self-excited oscillation. In processing the numerical data for this figure, the very high level isobar contours, corresponding to hydrodynamic waves around the jet core area are 'cut off' and the 'colors' are appropriately adjusted so that the acoustic waves are clearly displayed. The screech wavelength is about $1.6D$, well in line with experimental results (e.g. [8]). The shock cell structure in Fig. 13 is comparable to the experimental Schlierens in Fig. 12. Fig. 14 shows the PSD (power spectrum density) at the location $(x = 2.0, y = 6.0)$. It is seen that the spikes at the fundamental frequency and the subharmonics shoot out against the background noise, despite the low resolution. The fundamental frequency is estimated to be about $8,661$ Hz in this case, comparable to the experimental case - 8,525 Hz.

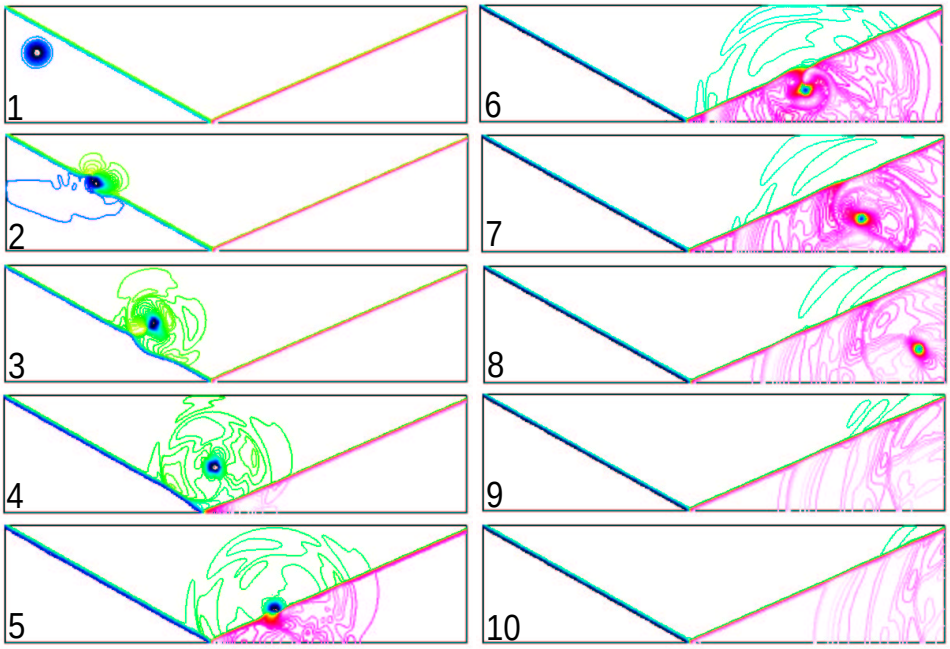

FIGURE 10. Multiple interactions of a strong vortex and shocks producing nonlinear acoustic waves.

4.3. Transonic resonance of a convergent-divergent(C-D) nozzle. The transonic resonance phenomenon of a C-D nozzle is a newly discovered jet noise [11] and is believed to be a precursor of such jet noises as the screech tones. Fig 15 is a sketch of the C-D nozzle transonic resonance problem. When the flow is at transonic speed, a shock Mach disc is formed at the nozzle throat. the disc vibrates like a diaphragm as a result of the self-sustaining oscillation in the flow, and triggers the quarter wave-length resonance of the divergent part of the nozzle, as if it were a circular duct with one end close. Fig. 16 shows that the computed frequencies agree very well with the experimental ones, including a stage jump where the resonance switches from fundamental frequency to the third harmonic. Furthermore, the two plots in Fig. 17 demonstrate the r.m.s. pressure fluctuation along the centerline of the divergent portion of the nozzle, showing clearly the fundamental frequency resonance (bottom plot) and third harmonic resonance (top plot). The numerical work thus helps to confirm the theory on the transonic resonance. The numerical work is detailed in [11].

4.4. the 3-D screech noise from a circular jet. The present problem is a 3-D version of the jet screech problem in §4.2. In order that the flow and and noise are truly three dimensional, the jet Mach number is set at $M_j = 1.42$ [9].

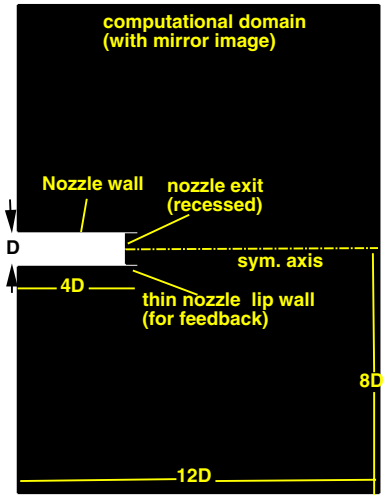

FIGURE 11. Geometry of the computational domain.

FIGURE 12. Schlieren picture from experiment (Panda), showing shock cells.

Approximately 3.7 million hexahedral cells are employed in the numerical solution. For a huge grid like this, parallel computation becomes necessary. A Linux PC cluster of 60 processors is used. Fig. 18 shows that the computed shock cell structure agrees well with the experimental one. For example, the shock cell spacing is about $1.28D$, D being the jet diameter at the nozzle exit. The radiated screech waves are in the flapping B mode, as shown in Fig. 19.

5. The Airframe Noise Problems

Airframe noise is an important noise source in aeroacoustics. Several airframe tone noise problems are considered in this section to demonstrate the capability of the CE/SE scheme.

5.1. The subsonic cavity noise problem. In this problem[12], a $M = 0.8$ subsonic flow passes over a cavity of aspect ratio 6.5. Tonal oscillations occur in a feedback cycle in which the vortices shed from the upstream lip of the cavity convect downstream and impinge on the other lip edge, generating acoustic waves that in turn propagate upstream to excite new vortices (Fig 20).

In the computational domain, 42,000 triangular elements are used in the unstructured grid, which is made from structured rectangular cells. Figure 21 depicts

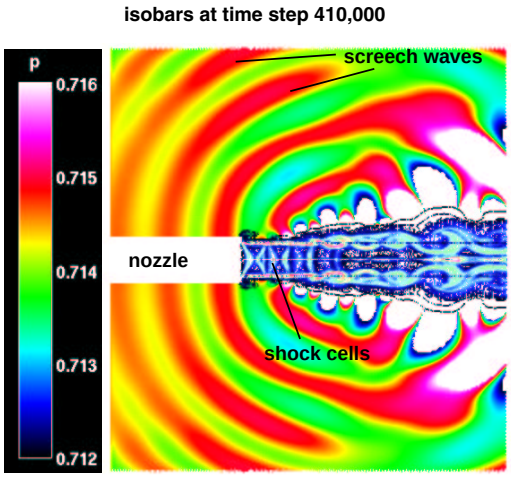

FIGURE 13. Screech wave radiation and shock cell structure (numerical Schlierens).

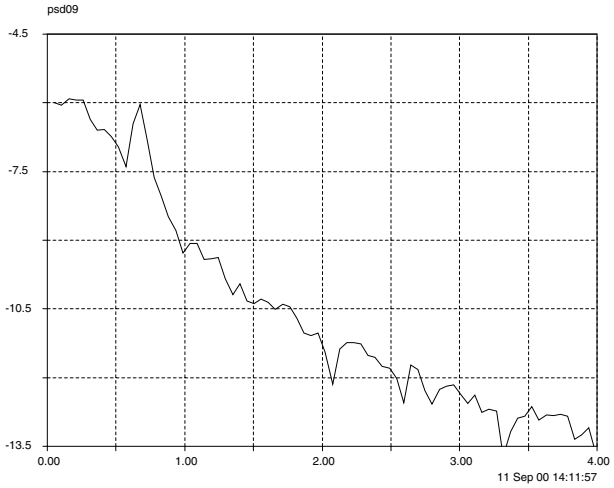

FIGURE 14. PSD at $(2, 6)$; x-axis: Strouhal number St, St=1 is equivalent to 13504 Hz.

with isobars where the acoustic waves are generated and propagate in a series of snapshots (1-12) in the near field of the cavity. Each snapshot is 3.6 (720 steps) unit apart in time. Initially, the flow conditions are set to be identical to the quiescent ambient flow. The boundary conditions are the appropriate types of NRBC except at the cavity walls, where no slip wall boundary condition is applied. No visible reflections are observed at the non-reflecting boundaries. At the inflow boundary, upstream propagating waves are well absorbed within 3-5 cells, without contaminating the interior domain. From an animation of the solution, the near field acoustic wave structure appears to be complicated and chaotic.

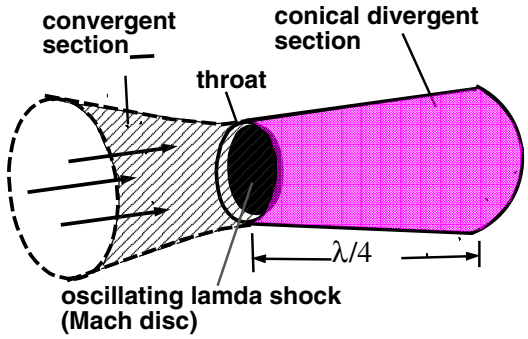

FIGURE 15. Transonic resonance of a C-D nozzle.

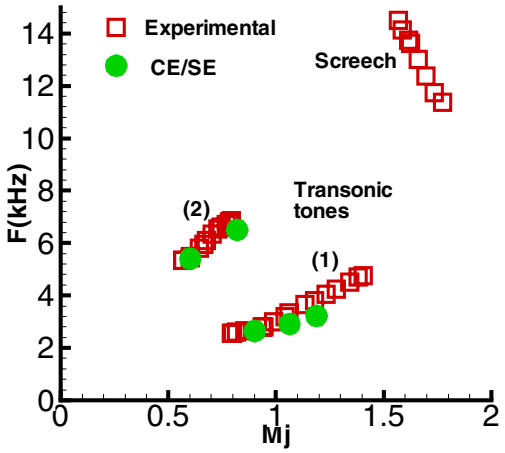

FIGURE 16. Frequency vs. jet Mach number M_j, showing frequency jumps (staging).

5.2. Flat plate trailing edge noise. In this last example, the noise generated by the von Karman vortex street downstream of a rectangular blunt slab is computed [13]. The flow Mach number is $M = 0.3$. Figure 22 illustrates the details of the computational domain. Initially, the entire field is set at the ambient flow. Then the inflow of $M = 0.3$ is imposed at the left boundaries. At the solid slab walls, no-slip condition is applied. The computation is totally carried out for 390,000 time steps. Time history at the data point as shown in Fig. 22 is recorded for FFT analysis. The power spectrum density (PSD) is shown in Fig. 23. As before, the $x-$ axis denotes the reduced frequency – the Strouhal numberSt. $St = 1$ is equivalent to a frequency of 13,504 Hz if the thickness of the slab is assumed to be one inch. The frequency at the lowest tone spike is 791 Hz, almost identical to Heinemann's experimental result [14].

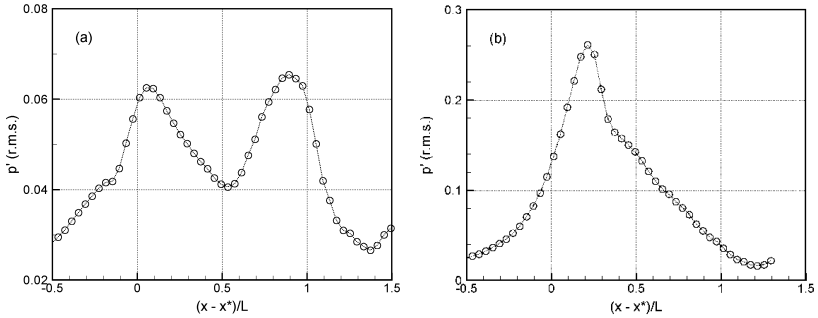

FIGURE 17. r.m.s. pressure fluctuation along the nozzle centerline.

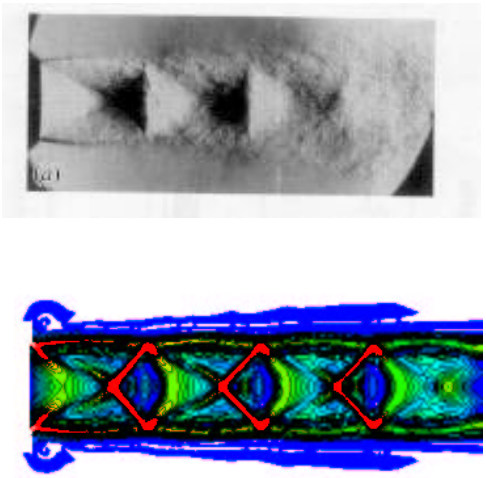

FIGURE 18. Comparison of experimental and numerical schlierens, showing shock cell structure. Note that the experimental result is a time-averaged one and the numerical one is instantaneous.

6. Concluding remarks

Through numerous numerical examples, the capability of the recent CE/SE schemes for aeroacoustics computations is demonstrated. The scheme features:

(1) naturally adapted to unstructured grid,

(2) high resolution, low dispersion, and low dissipation, despite its nominal 2nd order accuracy (in space and time),

(3) robust, treats the 'difficult' problems in a simple, effortless way, particularly appropriate for near field, non-linear aeroacoustics,

(4) the novel NRBC is simple, effective and truly multi-dimensional.

The CE/SE scheme thus is a viable tool for CFD and CAA, and in particular, for nonlinear aeroacoustics.

References

[1] Chang, S. C., "The Method of Space-Time Conservation Element and Solution Element—A New Approach for Solving the Navier-Stokes and

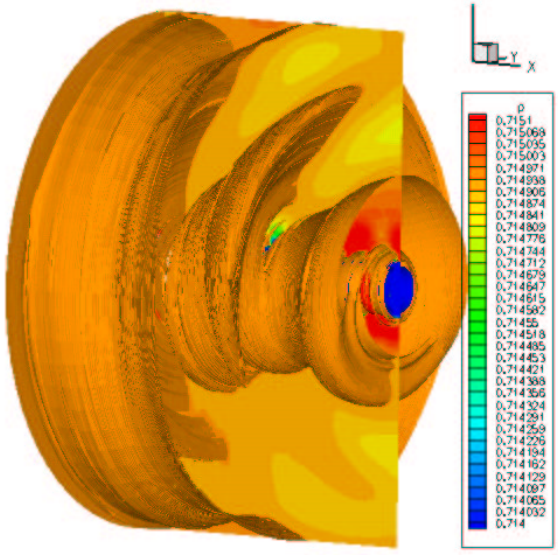

FIGURE 19. Pressure iso-surface at time step 120,000, showing helical radiating screech waves.

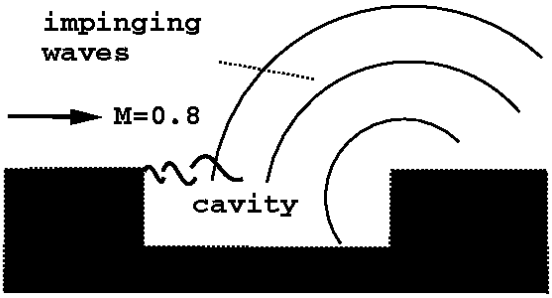

FIGURE 20. Sketch of the subsonic cavity noise problem.

Euler Equations," Journal of Computational Physics. v. 119, 295-324 (1995).

[2] Chang, S.-C., Wang, X.-Y. and Chow, C.-Y., "The Space-Time Conservation Element and Solution Element Method: A New High Resolution and Genuinely Multidimensional Paradigm for Solving Conservation Laws ", J. Comp. Phys. v.156, 89-136 (1999).

[3] Wang, X.Y. and Chang, S.C. "A 2D Non-splitting Unstructured Triangular Mesh Euler Solver Based on the Space-Time Conservation Element and Solution 'Element Method ", CFD Journal,vol. 8, pp.309-325, 1999. (1998).

[4] Hardin, J. C., Ristorcelli, and Tam, C. W. (Eds.), "ICASE/LaRC Workshop on Benchmark Problems in Computational Aeroacoustics", Hampton, VA. 1994, NASA CP 3300.

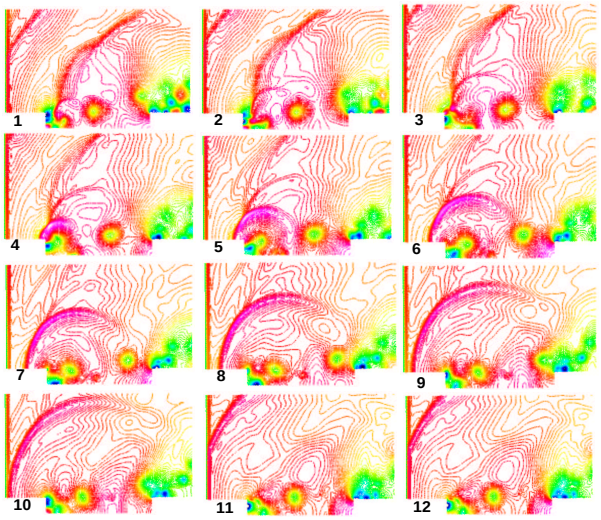

FIGURE 21. Isobar snapshots of the subsonic cavity flow field, showing upstream propagating nonlinear acoustic waves.

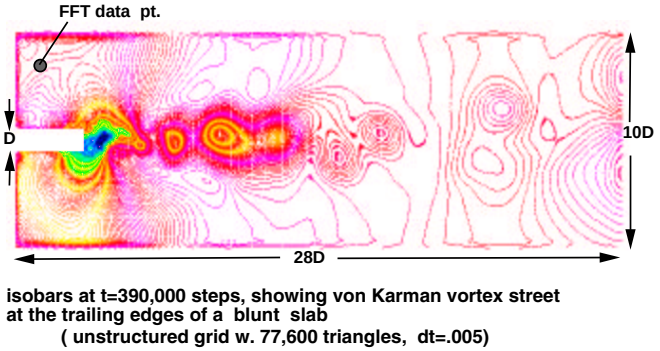

FIGURE 22. Isobar snapshot, showing von Karman vortex street downstream of the slab.

[5] Loh, Ching Y., Hultgren, Lennart S. and Sin-Chung Chang, "Computing Waves in Compressible Flow Using the Space-Time Conservation Element Solution Element Method," AIAA Paper 98-0369 (1998), also in AIAA Journal, vol. 39, pp794-801 (2001).

[6] Loh, C. Y., Hultgren, L. S., Wang,Xiao Y., Chang, S.-C. and Jorgenson, P. C. E., "Aeroacoustics Computation for Nearly fully Expanded Supersonic jets Using the CE/SE Method", AIAA Paper 2000-2010 (2000).

[7] Troutt, T. R. and McLaughlin, D. K., " Experiments on the flow and acoustic properties of a moderate-Reynolds-number supersonic jet", *J. Fluid Mech.*, vol. 116, pp. 123-156 (1982).

[8] Shih, S. H., Hixon, D. R. and Mankbadi, R. R., "Zonal Approach for Prediction of Jet Noise", *AIAA J.*, vol.13, pp. 745-752 (1997).

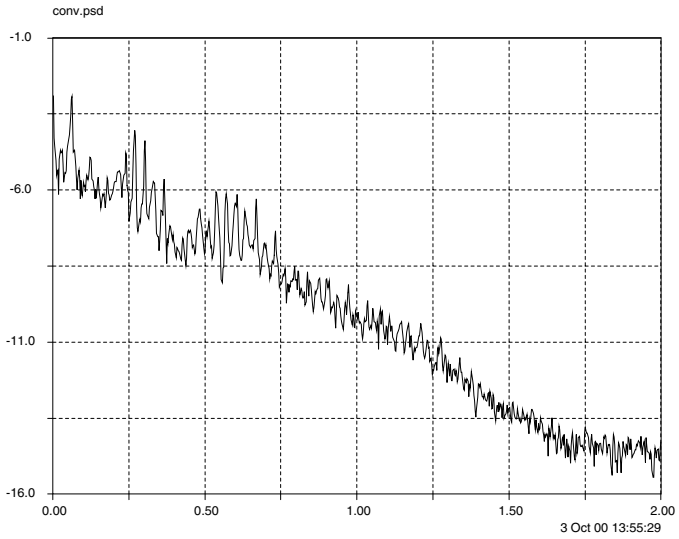

FIGURE 23. PSD at the FFT data point; x-axis: Strouhal number St, St=1 is equivalent to 13,504 Hz.

[9] Panda, J., "An experimental investigation of screech noise generation," *J. Fluid Mech.*, v. 378, pp. 71-96 (1998).

[10] Loh, C. Y., Hultgren, Lennart S. and Jorgenson, P. C. E., "Near Field Screech Noise Computation for an Underexpanded Supersonic Jet by the CE/SE method " AIAA Paper 2001-2252, May, 2001.

[11] Loh, C. Y., and K.B.M.Q. Zaman, "Numerical investigation of 'Transonic Resonance' with a Convergent-Divergent Nozzle", in AIAA Journal, Vol.40, No.12, pp. 2393-2401, 2002, also as AIAA Paper 2002-0077, Jan.,2002.

[12] Loh, C. Y., Wang,Xiao Y., Chang, S.-C. and Jorgenson, P. C. E., " Computation of Feedback Aeroacoustic System by the CE/SE Method" Presented at the 1st International CFD Conference, July, 2000, Kyoto, Japan.

[13] Loh, C. Y., "Near Field Trailing Edge Tone Noise Computation " AIAA Paper 2003-0365.

[14] H.J.Heinemann, O.Lawaczeck and K.A.Buterfisch, 'Karman vortices and their Frequency Determination in the Wakes of Profiles in the Sub-and Transonic Regime', Symposium Transonicum II, Goettingen, Germany, Sept. 1975; Springer-Verlag 1976, pp. 75-82.

REPORT DOCUMENTATION PAGE

Form Approved
OMB No. 0704-0188

1. AGENCY USE ONLY (*Leave blank*)	2. REPORT DATE	3. REPORT TYPE AND DATES COVERED
	June 2003	Final Contractor Report

4. TITLE AND SUBTITLE

Nonlinear Aeroacoustics Computations by the Space-Time CE/SE Method

5. FUNDING NUMBERS

WBS–22–708–90–25
NAS3–03072

6. AUTHOR(S)

Ching Y. Loh

7. PERFORMING ORGANIZATION NAME(S) AND ADDRESS(ES)

Taitech, Inc.
1430 Oak Court, Suite 301
Beaver Creek, Ohio 45430

8. PERFORMING ORGANIZATION REPORT NUMBER

E–13965

9. SPONSORING/MONITORING AGENCY NAME(S) AND ADDRESS(ES)

National Aeronautics and Space Administration
Washington, DC 20546–0001

10. SPONSORING/MONITORING AGENCY REPORT NUMBER

NASA CR—2003-212388

11. SUPPLEMENTARY NOTES

Prepared for the Regional Research Conference: Mathematical Methods in Nonlinear Wave Propagation cosponsored by the National Science Foundation and the Conference Board of the Mathematical Sciences, Greensboro, North Carolina, May 15–19, 2002. Project Manager, Richard A. Blech, Turbomachinery and Propulsion Systems Division, NASA Glenn Research Center, organization code 5880, 216–433–3657.

12a. DISTRIBUTION/AVAILABILITY STATEMENT

Unclassified - Unlimited
Subject Categories: 02 and 71 Distribution: Nonstandard

Available electronically at http://gltrs.grc.nasa.gov

This publication is available from the NASA Center for AeroSpace Information, 301–621–0390.

12b. DISTRIBUTION CODE

13. ABSTRACT ***(Maximum 200 words)***

The Space-Time Conservation Element and Solution Element Method, or CE/SE Method for short, is a recently developed numerical method for conservation laws. Despite its second order accuracy in space and time, it possesses low dispersion errors and low dissipation. The method is robust enough to cover a wide range of compressible flows: from weak linear acoustic waves to strong discontinuous waves (shocks). An outstanding feature of the CE/SE scheme is its truly multi-dimensional, simple but effective non-reflecting boundary condition (NRBC), which is particularly valuable for computational aeroacoustics (CAA). In nature, the method may be categorized as a finite volume method, where the conservation element (CE) is equivalent to a finite control volume (or cell) and the solution element (SE) can be understood as the cell interface. However, due to its careful treatment of the surface fluxes and geometry, it is different from the existing schemes. Currently, the CE/SE scheme has been developed to a matured stage that a 3-D unstructured CE/SE Navier-Stokes solver is already available. However, in the present review paper, as a general introduction to the CE/SE method, only the 2-D unstructured Euler CE/SE solver is chosen and sketched in section 2. Then applications of the 2-D and 3-D CE/SE schemes to linear, and in particular, nonlinear aeroacoustics are depicted in sections 3, 4, and 5 to demonstrate its robustness and capability.

14. SUBJECT TERMS	15. NUMBER OF PAGES
Nonlinear aeroacoustics; CE/SE method	21
	16. PRICE CODE

17. SECURITY CLASSIFICATION OF REPORT	18. SECURITY CLASSIFICATION OF THIS PAGE	19. SECURITY CLASSIFICATION OF ABSTRACT	20. LIMITATION OF ABSTRACT
Unclassified	Unclassified	Unclassified	